ROYAL SOCIETY
OF CHEMISTRY

CrystEngComm

Precursor Purity Effects on Solution-Based Growth of MAPbBr3 Single Crystals towards Efficient Radiation Sensing

Journal:	*CrystEngComm*
Manuscript ID	CE-ART-09-2018-001498.R1
Article Type:	Paper
Date Submitted by the Author:	12-Oct-2018
Complete List of Authors:	Tisdale, Jeremy; The University of Tennessee, Department of Materials Science and Engineering Smith, Travis; The University of Tennessee, Nuclear Engineering Salasin, John; The University of Tennessee, Department of Materials Science and Engineering Ahmadi, Mahshid; University of Tennessee, Materials Science and Engineering Johnson, Nathan; The University of Tennessee, Nuclear Engineering Ievlev, Anton; Oak Ridge National Laboratory, Center for Nanophase Materials Sciences Koehler, Michael; Joint Institute for Advanced Materials, University of Tennessee, Diffraction Facility Rawn, Claudia; The University of Tennessee, Department of Materials Science and Engineering Lukosi, Eric; University of Tennessee, Nuclear Engineering Hu, Bin; The University of Tennessee, Department of Materials Science and Engineering

SCHOLARONE™
Manuscripts

Precursor Purity Effects on Solution-Based Growth of MAPbBr$_3$ Single Crystals towards Efficient Radiation Sensing

Jeremy T. Tisdale*,[1], Travis Smith*,[2], John Robert Salasin[1], Mahshid Ahmadi[1], Nathan Johnson[2],

Anton V. Ievlev[3], Michael Koehler[1], Claudia J. Rawn[1], Eric Lukosi[2], and Bin Hu[1]

[1]Department of Materials Science and Engineering, University of Tennessee-Knoxville, Tennessee 37996-4545, USA

[2]Department of Nuclear Engineering, University of Tennessee-Knoxville, Tennessee 37996-4545, USA

[3]Center for Nanophase Materials Sciences, Oak Ridge National Laboratory, Oak Ridge, Tennessee 37831-6056, USA

*Both authors contributed equally to this work.

Corresponding Author: Dr. Bin Hu, bhu@utk.edu and Dr. Eric Lukosi, elukosi@utk.edu

KEYWORDS: Methylammonium lead tribromide; Single crystal; Radiation detection; Charge Collection; Boundary Trapping

ABSTRACT

Organometallic halide perovskite (OMHPs) single crystals have recently gained attention for high-energy radiation detection due to their low trap state densities, high bulk resistivities, excellent stopping power and cost-effective solution growth. An integral focus for radiation sensing materials is reduction of trap states to enhance charge transport properties. In this perspective, we investigate the use of high and low purity precursors for growth to understand impurity inclusion, as well as effects on structural properties due to impurities. Using both high purity and low purity precursors, we report minimal effects on impurity inclusion observed via Raman, ToF-SIMS and X-ray diffraction. Through SEM analysis, we observe that the particle size in the grown single crystal increased on average by a factor of two to five, when using high purity precursors. The microstructural changes affect recombination mechanisms, promoting longer charge carrier lifetimes (τ_{avg}), where time-resolved photoluminescence shows a large increase from $\tau_{avg} = 1.26 \times 10^{-6}\,s$ (low purity) to $\tau_{avg} = 1.18 \times 10^{-4}\,s$ (high purity). We further investigate the purity effects with alpha radiation detection, demonstrating that charge collection efficiency, observing an increase in charge collection by $32 \pm 30\%$ using the higher purity precursors. The microstructural differences in growth are herein proposed to be caused by nucleation from the impurities present in the solution, thereby adversely affecting the electronic properties of the $MAPbBr_3$ single crystals. In this perspective, we provide a deeper understanding of the effects of precursor purity on solution-based single crystal growth of OMHPs towards development of efficient radiation sensors and optoelectronic devices.

INTRODUCTION

In recent years, methylammonium lead halide perovskites (MAPbX$_3$: MA = CH$_3$NH$_3^+$, X = I$^-$, Br$^-$ or Cl$^-$) have gained attention for a variety of applications including, but not limited to, photovoltaics[1-6], photodetectors[7], lasing[8], light-emitting diodes[9] and more recently for high energy radiation sensors.[10-12] These materials have gained interest due to their tunable optical band gaps, desirable electronic properties, low cost and wide range of deposition techniques.[13-15] Specifically, single crystalline MAPbBr$_3$ has garnered attention due to its low trap state density and long carrier diffusion length.[13-15] Single crystalline MAPbBr$_3$ is grown using simple, low-cost, low-temperature, solution-based crystal growth techniques, with the growth process only taking hours to days to complete. For optoelectronic application and high energy radiation detection, an essential parameter for suitable materials relies on low trap and defect density. In this perspective, we investigate the effects of precursor purity on charge transport properties and structural changes in single crystals of MAPbBr$_3$. To study the impact that growth conditions have on the quality of MAPbBr$_3$ single crystals (desire low trap density and high charge carrier properties), it is important to understand similar studies on MAPbX$_3$ thin films processes, single crystal growth techniques for MAPbX$_3$, and mechanisms behind the crystal growth techniques.

Studies on MAPbI$_3$ thin films have shown that the purity of PbI$_2$ precursor used in the preparation of solutions for spin-coating and spray-coating has a large impact on the thin film properties and device performances. Chang, et al. observed that impurities can lower electron lifetime and increase the amount of non-radiative recombination in MAPbI$_3$ thin films.[16] They were able to reduce the amount of impurities in the active layer by using higher purity PbI$_2$ in the spin-coating solution and overall increased the power conversion efficiency (PCE) of MAPbI$_3$ solar cells by 3-4%. Similarly, Yao, et al. established that the purity of PbI$_2$ purity in spray-coating solutions had

a large impact on the crystallinity, grain size and grain boundaries in MAPbI$_3$ thin films for solar cells.[17] It was found that using higher purity PbI$_2$ precursor greatly increases the PCE of MAPbI$_3$ solar cells and eliminates hysteresis effects. Single crystalline MAPbBr$_3$ has commonly been grown using lower purity precursor materials, such as 98% PbBr$_2$.[11-15] These reports have shown excellent single crystalline quality and novel use in high-energy radiation detection; however, no reports have shown how the purity of precursor materials can affect the pertinent electronic properties of single crystals for high-energy radiation detection.

Several solution-based techniques have been studied for single crystal growth of organic-inorganic halide perovskite single crystals. A slow cooling method has been heavily studied for MAPbI$_3$ single crystal growth, where a seed crystal is placed in solution, and the solution is cooled slowly over the course of days to grow on the seeded crystal. However, this growth technique is only suitable for materials that have high solubility at high temperatures,[14,18,19] and the solubility of MAPbBr$_3$ is low at high temperatures. Therefore, growth of MAPbBr$_3$ single crystals commonly use anti-solvent vapor-assisted crystallization (ASC) and inverse temperature crystallization (ITC) techniques. The ASC method is efficient for synthesizing high quality crystals, but it is difficult to obtain large crystal sizes, limiting potential use in optoelectronic applications.[13] ITC has shown to be the best technique for growth of large, high quality MAPbBr$_3$ single crystals. The MABr and PbBr$_2$ precursors have high solubility in N,N-Dimethylformamide (DMF) at room temperature with a decrease in solubility as the temperature increases.[15,20,21] Understanding the mechanisms behind single crystal growth and its impact on electronic performance is a critical step in enhancing device performance. In solution-based growth, free parameters like precursor purity can have an impact on crystal quality (e.g., intrinsic defect minimization), causing significant effects on the electronic properties of the crystals. Impurities in the solvent and solute may incorporate

themselves in the crystal structure via interstitial and substitutional defects. Understanding the mechanisms of solution-based growth should help to identify how to properly control the growth conditions to minimize intrinsic and/or extrinsic defects to achieve higher-quality $MAPbBr_3$ single crystals.

In this report, we investigate the impact of precursor purity on the structural and electronic properties of single crystalline $MAPbBr_3$ using the ITC method for sensing and opto-electronic applications. We specifically studied if impurities were incorporated into the crystal structure during growth and whether increasing the purity of the precursors had a positive impact on single crystal quality. We also examined how the electronic properties of single crystalline $MAPbBr_3$ are modified with different precursor purities through charged particle detection.

EXPERIMENTAL

Growth of MAPbBr₃

Methylammonium lead bromide (MAPbBr₃) single crystals were grown using the ITC method.[17] To prepare the growth solution, methylammonium bromide and lead(II) bromide (PbBr₂) were mixed with a 1:1.25 (PbBr₂:MABr) in N,N-dimethylformamide (DMF). For lower purity stock materials, PbBr₂ (98%-Alfa Aesar) and MABr (98%-Sigma-Aldrich) were used for solution preparation. For high purity stock materials, PbBr₂ (99.999%, trace metals basis-Sigma-Aldrich) and MABr (99.5%-Osilla) were used for solution preparation. All materials used in the growth process were used as received. The solution was stirred for one hour at room temperature for dissolution and homogenization. The solution was then filtered using a 0.2 μm PTFE filter. After filtration, the solution was divided among vials in 2 mL quantities. The vials were placed in an oil bath at 75 °C. After growth, the samples were washed using dichloromethane (DCM).

Alpha Radiation Detection Device Fabrication

For alpha radiation detection, the MAPbBr₃ single crystals were mechanically polished using SiC films down to a 0.1 μm abrasive particle size. After polishing a 20 nm layer of C60 followed by an 8 nm layer of bathocuproine (BCP) were deposited on one side of the crystal. Then, 60 nm thick Cr electrodes were deposited on both faces. Cr has been used in previous studies using MAPbBr₃ for radiation detection[12] and has also been shown to exhibit Ohmic behavior.[22] All electrode layers were deposited via thermal evaporation.

Measurements Techniques

X-ray powder diffraction (XRD) was performed on a Malvern PANalytical Empyrean diffractometer setup in Bragg-Brentano geometry utilizing a PIXcel^{3D} area detector with 255 active channels with ~ 3 °2Θ of coverage. Samples were first characterized as-grown and then ground into a polycrystalline powder with an agate mortar and pestle and reanalyzed. The phase was identified using the ICDD PDF 4+ database and subsequent analysis using the Rietveld method was performed to obtain refined structural information using Malvern PANalytical's HighScore software. Time-resolved photoluminescence was performed using a 370 nm nanoLED photoexcitation source. The emission was measured at 575 nm with a time range of 5 μs. Raman spectroscopy was performed at liquid nitrogen temperature using a 473-nm pulse laser. The grating was set to 600 with the filter set to 0.01%. ToF-SIMS measurements were performed using a TOF.SIMS 5 NSC instrument (ION-TOF, Germany) using a Bi_3^+ primary ion beam with an energy of 30 keV, 30 nA current and 5 mm spot size. A sputter Cs^+ ion beam (1keV energy, 60 nA current and 20 mm spot size) was used to clean the sample surface before chemical imaging to minimize surface contamination manifesting itself in the collected ToF-SIMS spectra. Imaging was performed in positive ion detection mode. Alpha radiation spectra were collected by exposing the cathode of $MAPbBr_3$ detectors to a ^{210}Po radiation source and utilizing a pulse processing chain comprised of a CAEN A1422-F2-90 preamplifier, ORTEC 572A amplifier (shaping time of 10 μs), and an ORTEC ASPEC-927 multichannel analyzer. Alpha particle signal traces were collected by connecting a Cremat CR-110 preamplifier output to a 1.5 GHz Agilent Oscilloscope 54845A with a 1 MΩ input impedance. A custom LabVIEW program was used to capture 100 signal traces to analyze the rise time of each sample in response to alpha particles. The signal traces were averaged to minimize the effect of noise on the pulse shape. All measurements were completed in dark condition to avoid any interactions from light.

RESULTS & DISCUSSION

The samples compared were grown with two different precursor purities. Low purity refers to the single crystal grown with 98% PbBr2 and 98% MABr, while high purity refers to the single crystal grown with 99.999% PbBr2 and 99.5% MABr. XRD data at 300 K are shown for single crystalline (preferred orientation) and ground, polycrystalline powder $MAPbBr_3$ in Figures 1a and 1b, respectively. These patterns agree with previous literature for $MAPbBr_3$ single crystals and the data confirms the samples are single phase (ICDD# 01-084-9476).[23,24]
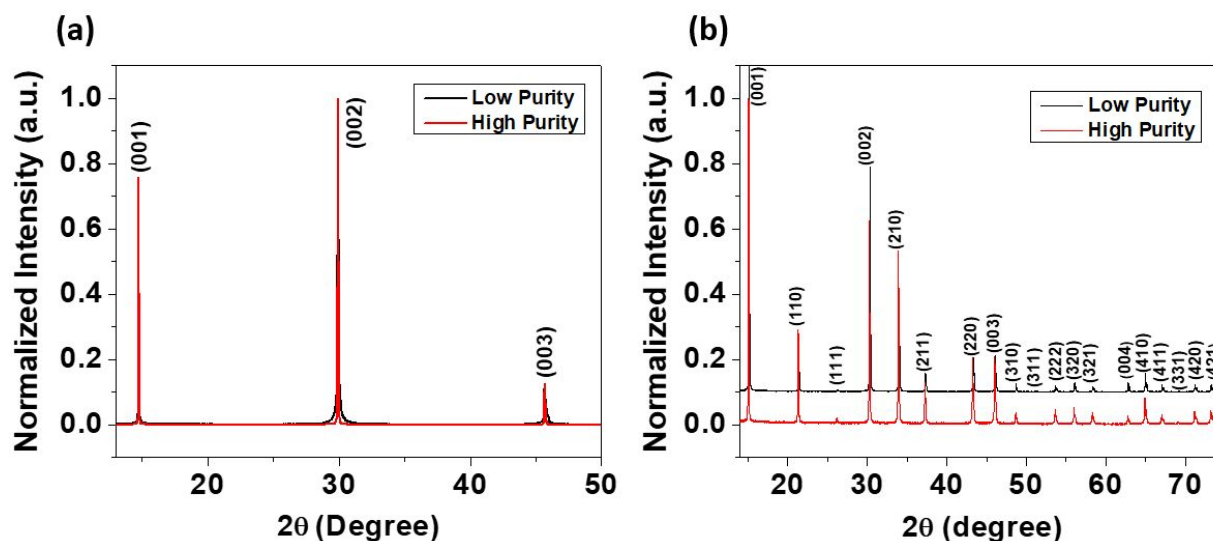
Figure 1. (a) XRD data collected on single crystals and (b) powder XRD for low and high purity grown single crystalline $MAPbBr_3$.

XRD diffraction on the as-grown, single crystal samples, synthesized from both the high and lower purity precursor materials, show preferred orientation in the *00l* crystal orientation. The FWHM deviates by only 0.001 °2θ between samples; however, the observed counts for the high purity precursor materials is orders of magnitude larger than the low purity sample correlated to a higher number of diffracted X-rays, suggesting a higher degree of crystallinity. This could also be the cause in the difference in tail characteristics due to microstructural Lorentzian broadening

observed in Figure 1a for the low purity crystal.[25,26] Powder XRD data was collected after grinding

the single crystals into polycrystalline samples, showing that all the characteristic peaks of the

cubic $Pm\overline{3}m$ space group are observed. When samples are ground, no difference in the peak shape

is observed, as crystallite size and preferred orientation differences are removed. The refined lattice

parameter of the high-purity phase is 5.9300(2) Å and for the low-purity phase is 5.9300(2) Å,

indicating no chemical strain that would be caused by ionic radii differences from impurities

leading to a change in lattice parameters. The crystalline quality is directly compared between low

and high purity-based samples via triple axis rocking curves, as shown in Figure S1. Rocking

curves are generated by rotating the sample to change the sample orientation while keeping the

angle of the incident beam constant. The width of the rocking curve directly measures the

crystalline quality of the single crystals, where curve broadness indicates crystalline disorder and

high mosaicity in the sample. By comparing the rocking curves in Figure S1, we show that the

high purity sample has highly textured crystalline quality, while the low purity sample shows

higher disorder by a broader FWHM of the main rocking curve peak, as well as plane tilting in the

sample observed by the presence of a second small peak.[27]

Raman spectroscopy was implemented to compare the vibrational MA^+ cation motions for low

and high purity samples to study any differences in the organic framework of the crystal structure.

The Raman spectra for low and high purity $MAPbBr_3$ single crystals are shown in Figure 2a. These

figures were used to compare the Raman spectra to literature values. Each spectrum shows great

signal to noise ratio, with sharp, high intensity peaks. We observe clear peak positions at 915, 975,

1251, 1425, 1480, and 1590 cm^{-1}, all related to different MA^+ cation motions as indicated in the

work reported by Wang et al.[24] For example, the 915 cm^{-1} peak is due to $CH_3NH_3^+$ rocking and

the 975 cm^{-1} peak is due to C-N stretching. The values of these peaks are in close agreement with reported Raman spectroscopy for single crystalline MAPbBr$_3$.[28-30]
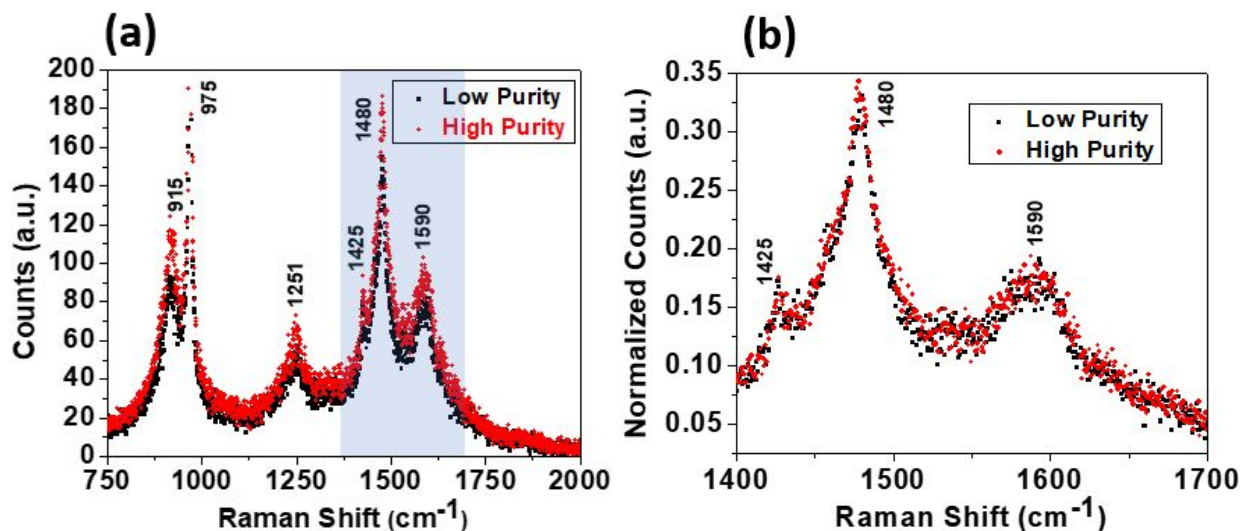
Figure 2. Raman spectroscopy for 98%-based and high purity single crystalline MAPbBr$_3$ from (a) 750-2000 cm^{-1} and (b) normalized spectra from 1400-1700 cm^{-1}. (blue shading in 2a shows area of interest for 2b)

To make a direct comparison between the low and high purity single crystal MAPbBr$_3$ samples, we normalized the Raman spectra and decreased the plotted shift range to the blue shaded region from Figure 2a, shown in Figure 2b. Figure S1 and Table S1 provide a quantitative analysis on the peak fitting for Raman spectroscopy to further examine changes between high and low purity crystals. The largest deviations occur in peak area, possibly indicating more disorder in the low purity samples. However, the peak positions are nearly identical, showing that the MA$^+$ cation motions were identical in each sample. Slight shifts in peak positions and widths, correlated to vibrational lifetimes, from reported values may arise from changes in sample crystallinity and defect composition. Therefore, due to the lack of any significant deviations when using lower purity precursor material, it is proposed that no large impurities are incorporated into the crystal structure that would alter the local environment of the organic framework. In Figure 2a, there is a slight difference observed, where the high purity sample has a slightly higher intensity for each

peak. From XRD and Raman spectroscopy, we show that using low purity precursor materials instead of higher purity precursor materials does not introduce any local or long range structural deviations correlated to the incorporation of impurities in single crystalline MAPbBr$_3$; however, using high precursors shows to have small effects on the long-range order of crystallites in the sample.
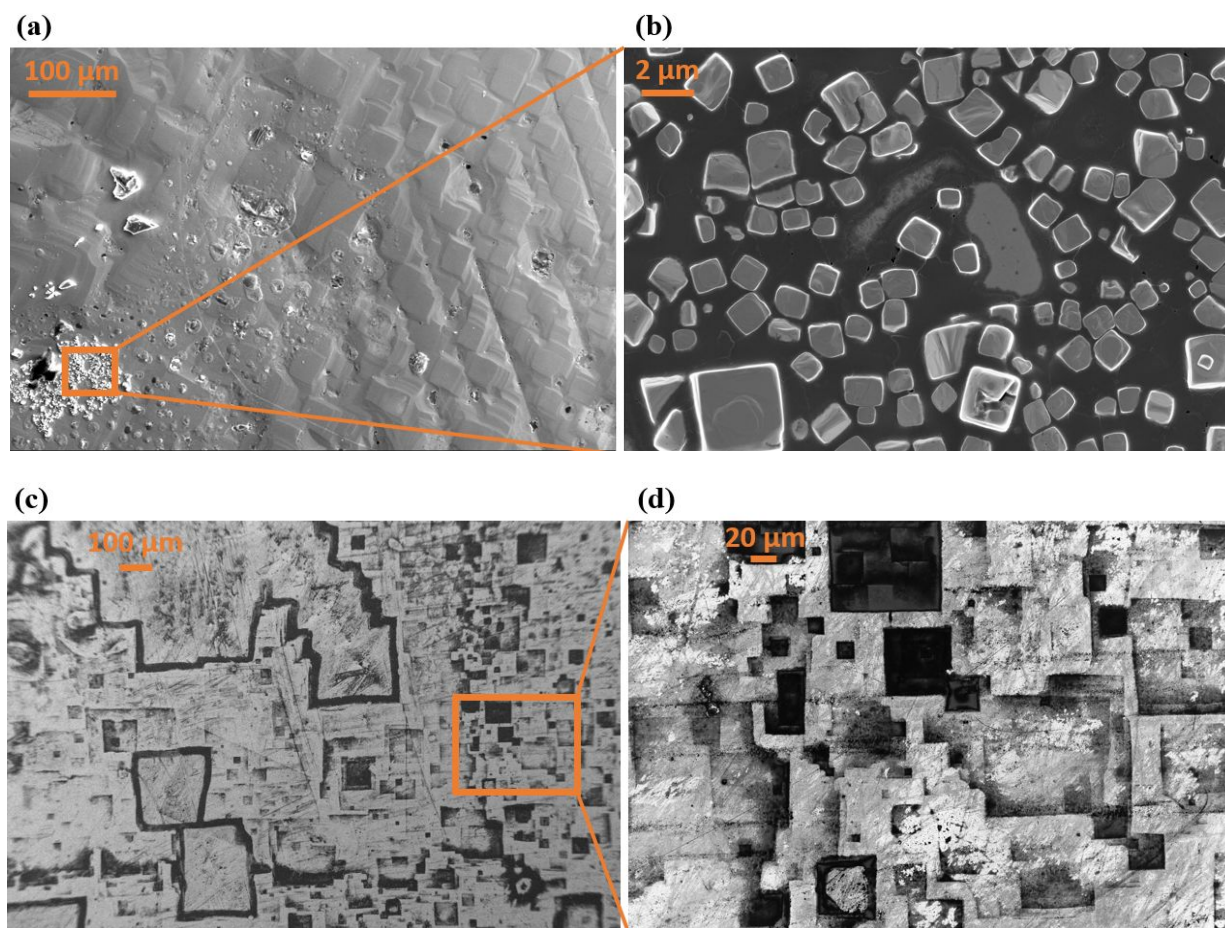
Figure 3. SEM images of (a,b) low purity MAPbBr$_3$ single crystals as-grown and (c,d) high purity MAPbBr$_3$ single crystals as-grown.

SEM (Scanning Electron Microscopy) images are shown in Figure 3 to further investigate the microstructural differences between low and high purity MAPbBr$_3$ single crystals. The growth of MAPbBr$_3$ single crystals was directly studied by Chen, F., et al., where they experimentally show how crystallites align together in a highly-textured orientation to form the final cubic single

crystal.[31] Further evidence is shown for this growth mechanism on the surface of the crystals, where square-like formations are observed as individual crystallites via SEM. Because solution-based growth of $MAPbBr_3$ forms single crystals through highly textured alignment of crystallites, it is important to understand impurity effects during growth, as impurities are able to act as nucleation sites, causing disorder in the alignment of crystallites.[32] In Figures 3a and 3b, the surface of the low purity sample is pictured. Here, it is important to note that the majority of the surface texture consists of crystallite boundaries on average of about 20-50 μm. Also, when the region of interest of Figure 3a is zoomed in, (as shown in Figure 3b) there are regions in the structure of even smaller crystallite boundaries ranging from approximately 200 nm to 2 μm. Therefore, it is observed that a high amount of nucleation occurs with a lower amount of continual crystal growth in the crystallites, correlated to the presence of defect centers introduced by impurities from the lower purity precursors. The SEM images of the high purity sample, shown in Figure 3c and 3d, show much larger crystallite sizes with an average of about 100 μm. When zoomed in, (as shown in Figure 3d) there are no regions of smaller, disordered crystallites, as seen in the low purity samples, and the average crystallite sizes are bigger than those of the low purity sample. This mixture of reduction in the size of the larger micron-sized crystallites and the presence of nano-sized crystallites give rise to the peak changes observed between high purity and low purity samples in XRD characterization. The decrease in crystallite size decreases the intensity of the diffracted X-rays and the presence of nano-sized crystallites leads to the Lorentzian broadening observed on the tails of the diffraction peaks. The disordered crystallites also give rise to more crystallite boundaries, which can act as trapping sites, adversely affecting electronic properties of the single crystal.

EDS (Figure S2) and ToF-SIMS (Figure S3) were used to ensure that the chemical composition remained homogenous throughout the surface of each sample despite the disorder and crystallite size of each region. EDS shows that the Pb to Br ratio was constant at a 1:3 ratio for both low and high purity samples regardless of the region of interest. ToF-SIMS also identifies a large peak for the methylammonium cation for both low and high purity crystals. This indicates that homogeneity of MAPbBr$_3$ is retained from small disordered crystallites to larger crystallite regions. Here, it is proposed that the changes in disorder of crystallites are caused by crystal growth in the presence of impurities. Although it is shown that impurities are not readily incorporated into the crystal structure, SEM shows that microstructural crystallite size and disorder changes when using low and high purity precursors. Using low purity precursors introduces more impurities in solution, which can act as nucleation sites.[32,33] Therefore, in low purity samples, it is observed that a higher rate of nucleation happens with a lower amount of contiguous crystal growth, while high purity samples have less nucleation and more crystal growth. Following these evaluations, we investigated the effect of precursor purity on the optical dynamics and electronic properties of single crystalline MAPbBr$_3$.
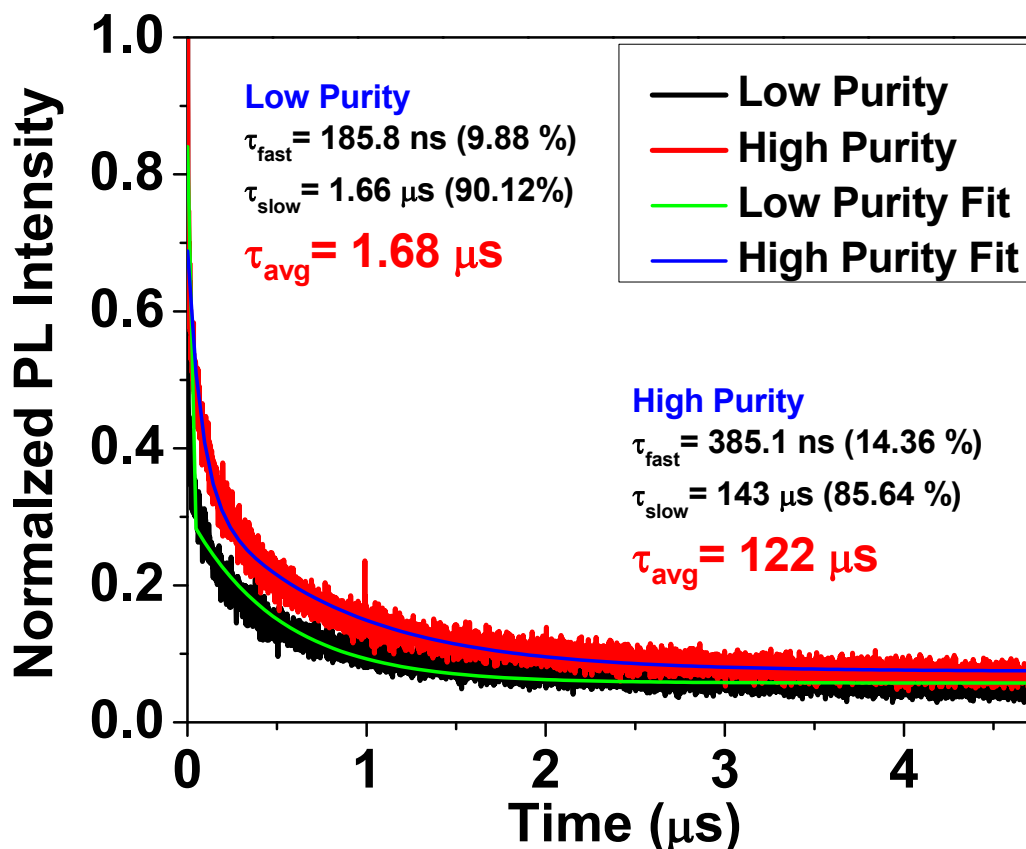
Figure 4. Normalized TRPL for MAPbBr$_3$ single crystals grown with low purity and high purity precursors.

Using time-resolved photoluminescence (TRPL), we investigated the optical dynamics in MAPbBr$_3$ single crystals grown with high and low purity precursors to study the carrier diffusion and recombination processes, shown in Figure 4.[34] A 370 nm nanoLED source was used for photoexcitation to probe the near-surface region of the samples.[35] For reproducibility of these measurements, three high purity and three low purity samples were measured and the average photogenerated carrier lifetime was calculated among the devices. For low purity, we calculated the average charge carrier lifetime as $\tau_{avg} = (1.26 \pm 0.36) \times 10^{-6}$ s, and for high purity, $\tau_{avg} = (1.18 \pm 0.12) \times 10^{-4}$ s. By comparing the average carrier lifetime, we gain valuable understanding on the carrier recombination process in the near-surface region, which directly affects carrier diffusion length. The high purity samples showed an increase of τ_{avg} by two orders

of magnitude, indicating less nonradiative recombination and charge carrier trapping in the high purity samples.[35] We attribute this increase in carrier lifetime to the increase in crystallite size and texture observed in the high purity single crystals. In the low purity samples, the smaller, disordered crystallite regions may act as recombination centers, introducing traps that reduce carrier lifetime and diffusion length in the single crystal. Meanwhile, we propose the larger, more textured crystallites in the high purity samples reduce the probability of nonradiative recombination and charge carrier trapping. Increasing the charge carrier lifetime is crucial for sensing and optoelectronic devices, where low trap-state density and long diffusion lengths are among the essential properties for efficient device performance.[13,14] In this perspective, we focus on the differences in crystallite boundaries during the growth process. However, deep and shallow trapping can also negatively impact the electronic properties. Therefore, in future work, further investigation into purity effects on the levels of defects generated due to impurities in precursors could provide a deeper understanding on defect generation and energies.

Lastly, the performance in application of single crystalline MAPbBr$_3$, grown with different precursor purities, is evaluated by comparing ^{210}Po alpha particle detection. For these measurements, the device structure was Cr(60 nm)/MAPbBr$_3$/C60(20 nm)/BCP(8 nm)/Cr(60 nm). This device structure is shown schematically in Figure S4a and has been used in previous literature for radiation detection.[12] All detectors were biased at -50 V on the Cr anode. The 5.3 MeV alpha spectra are shown for low purity and high purity-based MAPbBr$_3$ detectors in Figure 5a and Figure 5b, respectively, and an analysis of the collected results are provided in Table S2.
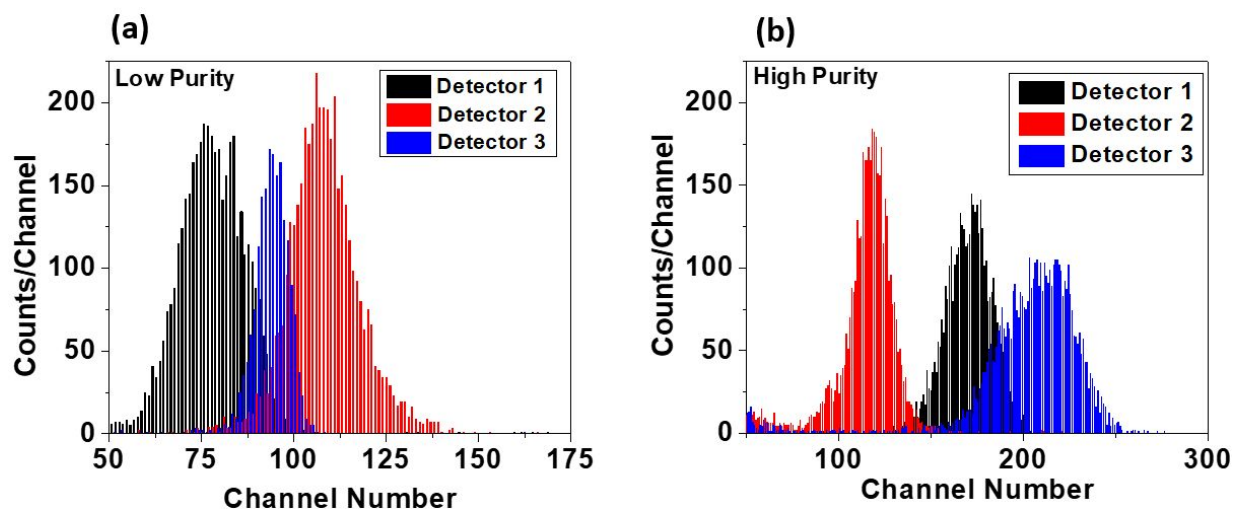
Figure 5. ^{210}Po alpha particle spectra collected at a -50 V bias for (a) low purity MAPbBr$_3$ detector and (b) high purity MAPbBr$_3$ detector.

The most apparent difference between the low purity and high purity detectors is the larger signal amplitude (H$_0$) from the higher purity samples. The average H$_0$ for the low purity and high purity detectors was calculated to be 92 ± 16 channels and 166 ± 45 channels, respectively. This corresponds to an average increase in signal amplitude by 80.44 ± 12.6%. The average energy resolution for the low purity and high purity detectors was calculated to be 18.13 ± 1.79% and 18.16 ± 7.25%, respectively. Although the average resolution is very similar, the larger standard deviation in the low purity samples can be attributed to the regions of nano-sized, disordered crystallites causing more microstructural differences between the low purity samples, whereas the crystallization of high purity samples is more consistent.

While an increase in signal amplitude, as measured by the multichannel analyzer, is typically attributed to a higher charge collection efficiency (CCE), the larger signal intensity could also result from an increase in sample mobility. The rise time of a MAPbBr$_3$ detector using low purity precursors has shown to exhibit a slow charge collection time, leading to a significant level of ballistic deficit.[36] As bias was increased across the sample, the increase in charge collection

observed was a combination of reduced charge carrier trapping and enhanced signal integrity through the amplifier. In this study, ballistic deficit could also play a significant role.

The preamplifier traces were evaluated on an oscilloscope to determine the charge collection time of each detector[37-39] and remove the ballistic deficit from the preamplifier using a cascade of partial deconvolutions.[40] The average of the 100 preamplifier traces collected for each low purity and high purity detector were aligned using a constant fraction discrimination algorithm in Matlab™ and the results are shown in Figure S4. In Equation 1, the integrated charge V_c, deconvolved from the single pole of the preamplifier, was determined at each time stamp i, where s is the sampling frequency of the oscilloscope, τ_p is the fall time of the preamplifier, and V_p is the uncorrected signal.

$$V_c(i) = V_p(i) + (1 - e^{-s/\tau_p}) \sum_{j=1}^{i-1} V_p(j) \qquad (2)$$

After deconvolving each of the pulses, it is shown that the high purity detectors collected an average of $32 \pm 30\%$ more charge at the time stamp corresponding to the maximum amplitude observed from the averaged preamplifier traces. We used this time stamp rather than the maximum charge observed to remove the effect of the much slower detrapped charge that manifests itself on the decaying tail of the preamplifier trace.

In addition, each of the low purity detectors has a signal rise that suggests there are multiple charge transport components involved during the primary signal rise. After a fast-initial rise, the slope of the rise decreases between 20 and 25 microseconds. We attribute this slow component of the rise time to charge trapping and detrapping. The high purity detectors do not show this same trapping behavior. In Table S2, drift mobility is calculated to compare three high purity and three low purity detectors. Assuming a flat electric field profile, $|\vec{v}|_{drift} = \mu |\vec{E}|$ may be used to calculate the

mobility, where $|\vec{v}|_{drift}$ is the observed 10% to 90% rise time from the averaged preamplifier traces. The average hole drift mobility for the high purity detectors was found to be 17.5 ± 1.9 $cm^2/_{V * s}$, and the hole drift mobility for the low purity detectors was 16.7 ± 1.9 $cm^2/_{V * s}$. While the difference in the hole mobility between the low purity and high purity samples helps explain the effect of potential error in evaluating the results if ballistic deficit is not taken into account, the larger average signal amplitude from the high purity samples clearly indicates that there is a reduction in charge trapping during the primary drift, enhancing charge collection. Although the energy resolution of the device did not increase using high purity precursors, the increase in CCE is a critical characteristic in efficient radiation sensing devices. By maximizing the CCE, the signal-to-noise ratio increases and enables sensing of lower energy X-rays and gamma rays that interact throughout the bulk of the MAPbBr$_3$ single crystals.

CONCLUSIONS

In summary, the effects of precursor purity on single crystalline MAPbBr$_3$ solution-based growth were deeply investigated. Although it is shown that impurities are not incorporated into the final crystal structure, impurities do alter the microstructure by acting as nucleation sites, which are shown to inhibit larger grain growth and alignment by increasing the amount and reducing the size of crystallites in the single crystal. We found that using high purity precursors increased the size of crystallites, yielding a higher photogenerated charge carrier lifetime by two orders of magnitude. The increase in carrier lifetime indicates a lower probability of nonradiative recombination and charge carrier trapping, thereby increasing the diffusion length of charge carriers due to less trap states at crystallite boundaries in the near-surface region. Further, through alpha particle sensing, the impact of precursor purity is evident on the charge transfer properties, where crystal growth using higher purity precursors yields higher charge collection efficiency. Therefore, we propose that although impurities are not incorporated into the final crystal structure in solution-based growth, the presence of impurities during the growth clearly affects the quality of single crystalline MAPbBr$_3$ via crystallite boundaries, negatively affecting electronic properties and decreasing device performance. In this perspective, we demonstrate the use of high purity precursors to enhance charge transfer properties towards developing efficient high energy radiation sensors and optoelectronic devices.

NOTES

The authors declare no competing financial interest.

DISCLAIMER

The views and conclusions contained in this document are those of the authors and should not be interpreted as necessarily representing the official policies, either expressed or implied, of the U.S. Department of Homeland Security.

REFERENCES

1.   Docampo, P., Ball, J. M., Darwich, M., Eperon, G. E. & Snaith, H. J. Efficient

        organometal trihalide perovskite planar-heterojunction solar cells on flexible

        polymer substrates. Nat. Commun. **2013**, 4, 2761, 1-6.

2.   Kim, H.-S.; Mora-Sero, I.; Gonzalez-Pedro, V.; Fabregat-Santiago, F.; Juarez-Perez, E.
        J.; Park, N.-G.; Bisquert, J., Mechanism of carrier accumulation in perovskite thin-
        absorber solar cells. *Nature Communications* **2013,** *4*, 2242, 1-7.

3.   Stranks, S. D.; Eperon, G. E.; Grancini, G.; Menelaou, C.; Alcocer, M. J. P.; Leijtens, T.;
        Herz, L. M.; Petrozza, A.; Snaith, H. J., Electron-Hole Diffusion Lengths Exceeding 1
        Micrometer in an Organometal Trihalide Perovskite Absorber. *Science* **2013,** *342* (6156),
        341-344.

4.   Mei, A.; Li, X.; Liu, L.; Ku, Z.; Liu, T.; Rong, Y.; Xu, M.; Hu, M.; Chen, J.; Yang, Y.;
        Grätzel, M.; Han, H., A hole-conductor–free, fully printable mesoscopic perovskite solar
        cell with high stability. *Science* **2014,** *345* (6194), 295-298.

5.   Nie, W.; Tsai, H.; Asadpour, R.; Blancon, J.-C.; Neukirch, A. J.; Gupta, G.; Crochet, J. J.;
        Chhowalla, M.; Tretiak, S.; Alam, M. A.; Wang, H.-L.; Mohite, A. D., High-efficiency
        solution-processed perovskite solar cells with millimeter-scale grains. *Science* **2015,** *347*
        (6221), 522-525.

6.   Choi, J.J., Yang, X., Norman, Z.M., Billinge, S.J.L. & Owen, J.S. Structure of

        methylammonium lead iodide within mesoporous titanium dioxide: active

        material in high-performance perovskite solar cells. Nano Lett. **2014**, 14, 127–133.

7.   Ahmadi, M.; Wu, T.; Hu, B., A Review on Organic–Inorganic Halide Perovskite
        Photodetectors: Device Engineering and Fundamental Physics. *Advanced Materials* **2017,**
        29 (41), 1605242, 1-24.

8.   Xing, G.; Mathews, N.; Lim, S. S.; Yantara, N.; Liu, X.; Sabba, D.; Grätzel, M.;
        Mhaisalkar, S.; Sum, T. C., Low-temperature solution-processed wavelength-tunable
        perovskites for lasing. *Nature Materials* **2014,** *13*, 476-480.

9.   Tan, Z.-K.; Moghaddam, R. S.; Lai, M. L.; Docampo, P.; Higler, R.; Deschler, F.; Price,
        M.; Sadhanala, A.; Pazos, L. M.; Credgington, D.; Hanusch, F.; Bein, T.; Snaith, H. J.;
        Friend, R. H., Bright light-emitting diodes based on organometal halide perovskite.
        Nature Nanotechnology **2014,** *9*, 687-692.

10.   Yakunin, S.; Dirin, D. N.; Shynkarenko, Y.; Morad, V.; Cherniukh, I.; Nazarenko, O.;
        Kreil, D.; Nauser, T.; Kovalenko, M. V., Detection of gamma photons using solution-

grown single crystals of hybrid lead halide perovskites. *Nature Photonics* **2016**, *10*, 585-589.

11.   Wei, H.; Fang, Y.; Mulligan, P.; Chuirazzi, W.; Fang, H.; Wang, C.; Ecker, B. R.; Gao, Y.; Loi, M. A.; Cao, L.; Huang, J., Sensitive X-Ray Detectors Made of Methylammonium Lead Tribromide Perovskite Single Crystals. *Nature Photonics* **2016**, 1-7.

12.   Xu, Q.; Wei, H.; Wei, W.; Chuirazzi, W.; DeSantis, D.; Huang, J.; Cao, L., Detection of Charged Particles with a Methylammonium Lead Tribromide Perovskite Single Crystal. Nuclear Instruments and Methods in Physics Research Section A: Accelerators, Spectrometers, Detectors and Associated Equipment **2017**, 848, 106-108.

13.   Shi, D.; Adinolfi, V.; Comin, R.; Yuan, M.; Alarousu, E.; Buin, A.; Chen, Y.; Hoogland, S.; Rothenberger, A.; Katsiev, K.; Losovyj, Y.; Zhang, X.; Dowben, P. A.; Mohammed, O. F.; Sargent, E. H.; Bakr, O. M., Low trap-state density and long carrier diffusion in organolead trihalide perovskite single crystals. *Science* **2015**, *347* (6221), 519-522.

14.   Dong, Q.; Fang, Y.; Shao, Y.; Mulligan, P.; Qiu, J.; Cao, L.; Huang, J., Electron-Hole Diffusion Lengths >175 Um in Solution-Grown Ch3nh3pbi3 Single Crystals. Sciencexpress **2015** 967-970.

15.   Saidaminov, M. I.; Abdelhady, A. L.; Murali, B.; Alarousu, E.; Burlakov, V. M.; Peng, W.; Dursun, I.; Wang, L.; He, Y.; Maculan, G., High-Quality Bulk Hybrid Perovskite Single Crystals within Minutes by Inverse Temperature Crystallization. Nature communications **2015**, 6, 7586, 1-6.

16.   Chang, J.; Zhu, H.; Li, B.; Isikgor, F. H.; Hao, Y.; Xu, Q.; Ouyang, J., Boosting the performance of planar heterojunction perovskite solar cell by controlling the precursor purity of perovskite materials. *Journal of Materials Chemistry A* **2016**, *4* (3), 887-893.

17.   Yao, J.; Yang, L.; Cai, F.; Yan, Y.; Gurney, R. S.; Liu, D.; Wang, T., The impacts of PbI2 purity on the morphology and device performance of one-step spray-coated planar heterojunction perovskite solar cells. *Sustainable Energy & Fuels* **2018**, *2* (2), 436-443.

18.   Dang, Y.; Liu, Y.; Sun, Y.; Yuan, D.; Liu, X.; Lu, W.; Liu, G.; Xia, H.; Tao, X., Bulk crystal growth of hybrid perovskite material CH3NH3PbI3. *CrystEngComm* **2015**, *17* (3), 665-670.

19.   Lian, Z.; Yan, Q.; Lv, Q.; Wang, Y.; Liu, L.; Zhang, L.; Pan, S.; Li, Q.; Wang, L.; Sun, J.-L., High-Performance Planar-Type Photodetector on (100) Facet of MAPbI3 Single Crystal. *Scientific Reports* **2015**, *5*, 16563, 1-10.

20.   Liu, Y.; Yang, Z.; Cui, D.; Ren, X.; Sun, J.; Liu, X.; Zhang, J.; Wei, Q.; Fan, H.; Yu, F.; Zhang, X.; Zhao, C.; Liu, S., Two-Inch-Sized Perovskite CH3NH3PbX3 (X=Cl, Br, I) Crystals: Growth and Characterization. *Advanced Materials* **2015**, 1-8.

21.   Han, Q.; Bae, S.-H.; Sun, P.; Hsieh, Y.-T.; Yang, Y.; Rim, Y. S.; Zhao, H.; Chen, Q.; Shi, W.; Li, G.; Yang, Y., Single Crystal Formamidinium Lead Iodide (FAPbI3): Insight into the Structural, Optical, and Electrical Properties. *Advanced Materials* **2016,** *28* (11), 2253-2258.

22.   Tisdale, J. T.; Muckley, E.; Ahmadi, M.; Smith, T.; Seal, C.; Lukosi, E.; Ivanov, I. N.; Hu, B., Dynamic Impact of Electrode Materials on Interface of Single-Crystalline Methylammonium Lead Bromide Perovskite. *Advanced Materials Interfaces* **2018,** *5* (18), 1800476.

23.   Peng, W.; Wang, L.; Murali, B.; Ho, K.-T.; Bera, A.; Cho, N.; Kang, C.-F.; Burlakov, V. M.; Pan, J.; Sinatra, L.; Ma, C.; Xu, W.; Shi, D.; Alarousu, E.; Goriely, A.; He, J.-H.; Mohammed, O. F.; Wu, T.; Bakr, O. M., Solution-Grown Monocrystalline Hybrid Perovskite Films for Hole-Transporter-Free Solar Cells. *Advanced Materials* **2016,** *28* (17), 3383-3390.

24.   Wang, K.-H.; Li, L.-C.; Shellaiah, M.; Wen Sun, K., Structural and Photophysical Properties of Methylammonium Lead Tribromide (MAPbBr3) Single Crystals. *Scientific Reports* **2017,** *7* (1), 13643, 1-14.

25.   Kaduk, J.A.; Reid, J.W., Typical values of Rietveld instrument profile coefficients. *Powder Diffraction* **2011**, *26*, 1, 88-94.

26.   S. Speakman, Estimating Crystallite Size Using XRD (MIT Center for Materials Science and Engineering, March 8, 2008), http://prism.mit.edu/xray/CrystalSizeAnalysis.ppt (accessed June 27, 2018).

27.   Alexander, W.; Sandoval, J.; Van Den Berg, L., Characterization of strain and crystallographic defects in HgI 2 single crystals. *Proceedings of SPIE* **2004**, 5540, 1-10.

28.   Park, N.-G., Perovskite Solar Cells: An Emerging Photovoltaic Technology. *Materials Today* **2015**, *18*, 65-72.

29.   Dang, Y.; Ju, D.; Wang, L.; Tao, X., Recent Progress in the Synthesis of Hybrid Halide Perovskite Single Crystals. *CrystEngComm* **2016**, *18*, 4476-4484.

30.   Leguy, A. M. A.; Goñi, A. R.; Frost, J. M.; Skelton, J.; Brivio, F.; Rodríguez-Martínez, X.; Weber, O. J.; Pallipurath, A.; Alonso, M. I.; Campoy-Quiles, M.; Weller, M. T.; Nelson, J.; Walsh, A.; Barnes, P. R. F., Dynamic disorder, phonon lifetimes, and the assignment of modes to the vibrational spectra of methylammonium lead halide perovskites. *Physical Chemistry Chemical Physics* **2016,** *18* (39), 27051-27066.

31. Chen, F.; Xu, C.; Xu, Q.; Zhu, Y.; Zhu, Z.; Liu, W.; Dong, X.; Qin, F.; Shi, Z., Structure Evolution of CH3NH3PbBr3 Single Crystal Grown in N,N-Dimethylformamide Solution. *Crystal Growth & Design* **2018,** *18* (5), 3132-3137.

32. Ginde, R. M.; Myerson, A. S., Effect of Impurities on Cluster Growth and Nucleation. *Journal of Crystal Growth* **1993**, *126*, 216-222.

33. De Yoreo, J. J.; Vekilov, P. G. In *Reviews in Mineralogy and Geochemistry: Biomineralization*; Dove, P. M., De Yoreo, J. J., Weiner, S., Eds.; Mineralogical Society of America: Washington, DC, **2003**; Vol. 54, p 57.

34. Lu, H.; Zhang, H.; Yuan, S.; Wang, J.; Zhan, Y.; Zheng, L., An optical dynamic study of MAPbBr3 single crystals passivated with MAPbCl3/I3-MAPbBr3 heterojunctions. *Physical Chemistry Chemical Physics* **2017,** *19* (6), 4516-4521.

35. Yamada, Y.; Yamada, T.; Phuong, L. Q.; Maruyama, N.; Nishimura, H.; Wakamiya, A.; Murata, Y.; Kanemitsu, Y., Dynamic Optical Properties of CH3NH3PbI3 Single Crystals As Revealed by One- and Two-Photon Excited Photoluminescence Measurements. *Journal of the American Chemical Society* **2015,** *137* (33), 10456-10459.

36. Lukosi, E.; Smith, T.; Tisdale, J.T.; Hamm, D.; Seal, C.; Hu, B.; Ahmadi, M., (Unpublished Results) Methylammonium Lead Tribromide Semiconductors: Ionizing Radiation Detection and Electronic Properties. **2018**.

37. Erickson, J. C.; Yao, H. W.; James, R. B.; Hermon, H.; Greaves, M., Time of flight experimental studies of CdZnTe radiation detectors. *Journal of Electronic Materials* **2000,** *29* (6), 699-703.

38. Zanio, K. R.; Akutagawa, W. M.; Kikuchi, R., Transient Currents in Semi-Insulating CdTe Characteristic of Deep Traps. *Journal of Applied Physics* **1968,** *39* (6), 2818-2828.

39. Liu, X.; Zhang, H.; Zhang, B.; Dong, J.; Jie, W.; Xu, Y., Charge Transport Behavior in Solution-Grown Methylammonium Lead Tribromide Perovskite Single Crystal Using α Particles. *The Journal of Physical Chemistry C* **2018,** *122* (26), 14355-14361.

40. A. Georgiev and W. Gast, "Digital Pulse Processing in High Resolution, High Throughput, Gamma-Ray Spectroscopy," *IEEE Transactions on Nuclear Science, 1993,* 40, 4, 770-779.